Intermetallics 141 (2022) 107432

Contents lists available at ScienceDirect

Intermetallics

journal homepage: www.elsevier.com/locate/intermet

Structure, mechanical properties and nanocrystallization of (FeCoCrNi)-(B, Si) high-entropy metallic glasses

S. Leila Panahi [a], Jordina Fornell [b], Catalin Popescu [c], Eloi Pineda [a,d,e], Jordi Sort [b,f], Pere Bruna [a,d,e,*]

[a] Departament de Física, Universitat Politècnica de Catalunya - BarcelonaTech, 08019, Barcelona, Spain
[b] Departament de Física, Facultat de Ciències, Universitat Autònoma de Barcelona, 08193, Bellaterra, Spain
[c] CELLS-ALBA Synchrotron Light Facility, Cerdanyola, Barcelona, 08290, Spain
[d] Institut de Tècniques Energètiques, Universitat Politècnica de Catalunya – BarcelonaTech, 08028, Barcelona, Spain
[e] Barcelona Research Center in Multiscale Science and Engineering, Universitat Politècnica de Catalunya - BarcelonaTech, 08019, Barcelona, Spain
[f] Institució Catalana de Recerca i Estudis Avançats, 08010, Barcelona, Spain

ARTICLE INFO

Keywords:
High-entropy alloys
Synchrotron radiation
Nanoindentation
Metallic glass

ABSTRACT

New high-entropy metallic glasses were produced by adding B and Si to the $Fe_{25}Co_{25}Cr_{25}Ni_{25}$ high entropy alloy. Extremely hard materials were obtained by inducing structural relaxation and nanocrystallization in the original amorphous metals. In this work we study the effects of the composition and annealing treatments on the structure and the mechanical properties. The changes in structure during heating treatments were determined by in situ synchrotron X-ray diffraction and the mechanical behavior was studied by nanoindentation. The mechanical properties of the as-quenched glasses were tuned through the annealing treatments, obtaining amorphous/nanocrystalline composites appropriate for highly demanding, wear resistance applications. The relative amount of B and Si is shown to determine the main nanocrystalline phase, FCC or BCC, which has a key influence on the mechanical properties.

1. Introduction

The necessity of new metals with unique properties has become more important than ever for the development of demanding, new applications, ranging from medical implants to ship surface coatings and sport equipment [1]. Among the new type of alloys recently designed, high entropy alloys (HEA) stand out due to the combination of high hardness, high strength, high corrosion resistance and high temperature softening resistance [2–5]. HEAs can be used as coatings [6] and in new manufacturing technologies [7]. In turn, metallic glasses (MG) have been thoroughly studied in recent years due to their distinctive mechanical, chemical and magnetic properties [8]. The possibility of combining the excellent properties of these two types of alloys, rendering the so-called high-entropy metallic glasses (HEMG), is an interesting strategy to obtain new materials with further optimized performance. Some steps in this direction have recently been done in the FeCoCrNi system. Li et al. [9] produced this HEA with a high undercooling obtaining the enhancement of its compressive yield strength. Xiao et al. [10], through the addition of Mn, produced a crystalline/amorphous dual phase with improved hardness. Medina et al. [11] explained the improvement of the mechanical properties of the FeCoCrNiMn HEA after the addition of C by the shift from a crystalline to an amorphous structure. Thus, the production of HEA with a total or partial amorphous structure is revealed as a practical way to widen the range of materials and compositions with tailored properties.

High entropy alloys are multicomponent alloys, with a concentration between 5 and 35 at% of each element, and large entropy of mixing [12]. In comparison to multicomponent alloys forming intermetallic compounds and complex microstructures, which make them brittle and difficult to process, HEAs tend to be solid solutions with body-centered (BCC) or face-centered (FCC) cubic structures. Metallic glasses are also multicomponent alloys, but they retain the amorphous structure when quenching from the liquid state. Large, negative values of mixing enthalpy and relatively large atomic size differences tend to stabilize the liquid structure and inhibit crystallization, thus promoting glass-forming ability [13]. HEAs and MGs share in common the presence of a single structural phase, crystalline or amorphous respectively, with the different components of the alloy being dissolved in the structure.

* Corresponding author. Departament de Física, Universitat Politècnica de Catalunya - BarcelonaTech, 08019, Barcelona, Spain.
E-mail address: pere.bruna@upc.edu (P. Bruna).

https://doi.org/10.1016/j.intermet.2021.107432
Received 16 September 2021; Received in revised form 14 November 2021; Accepted 27 November 2021
Available online 3 December 2021

While in HEA the different components are usually of similar atomic size, in order to promote the crystallization of a solid solution, the MG-forming systems contain elements with dissimilar atomic sizes in order to hinder crystallization [14].

With the aim of exploring new materials with exceptional properties, we produced rapidly quenched alloys combining the equiatomic, HEA $Fe_{25}Co_{25}Cr_{25}Ni_{25}$ composition with B and Si, which are elements known to enhance glass-forming ability. By systematically changing the content of B and Si we determined the range of compositions with higher glass-forming ability as detailed in [15], producing new HEMGs. Fig. 1 summarizes the results of this previous study [15] together with some new compositions produced since then. All the materials were produced by rapid solidification with exactly the same production parameters, thus expecting the same quenching rate. Fig. 1 shows a clear zone in the ternary HEA-B-Si diagram where glass forming ability is high enough to obtain completely amorphous alloys. In this work, in order to study the effect of composition, glass relaxation and crystallization on the mechanical properties we selected the compositions with best glass-forming ability, emphasized with circles in Fig. 1.

One of the most used techniques to study the mechanical properties and the deformation process at the nanoscale is nanoindentation. This technique offers many advantages and it requires only small volumes of test material [16]. Several mechanical properties related to the elastic and plastic deformation response can be assessed from the load-displacement (P-h) curves recorded during the nanoindentation process [17]. The method of Oliver and Pharr [18] allows extracting the hardness and the Young's modulus from parameters measured directly on the unloading part of the P-h curve: the load at the peak (P_{max}), the maximum penetration depth (h_{max}), the residual depth after unloading (h_r) and the slope of the upper portion of the unloading curve, known as the contact stiffness (s_w). The particular response of the material depends on many factors like the crystal structure, the chemical composition and/or the microstructure [19]. Moreover, in some materials, phenomena like pile-up or sink-in, that depend only on plastic properties [20], can occur, yielding differences in the contact area.

In this work the mechanical properties of the new HEMGs [15] are studied by nanoindentation and they are correlated with their crystallization behavior studied by in-situ X-ray diffraction in a synchrotron source. Different microstructural states are obtained by applying thermal treatments on the as-quenched amorphous samples. The tailoring of the structural and microstructural state achieves an outstanding improvement of the mechanical properties.

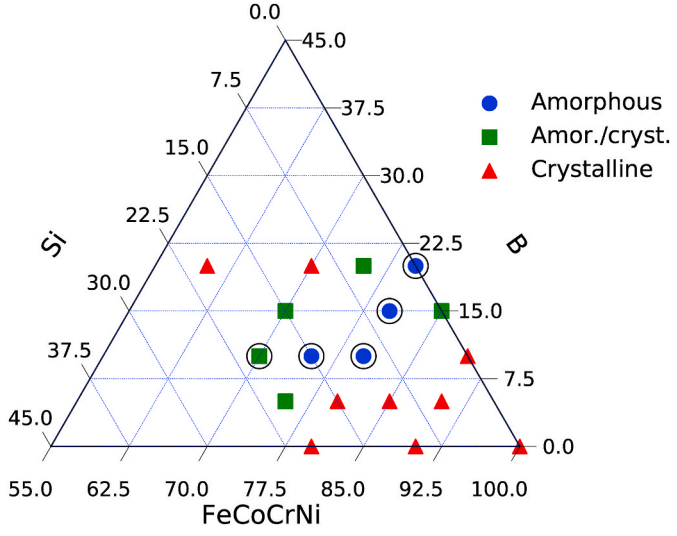

Fig. 1. Compositions of the produced materials, detailing their amorphous (blue circles), crystalline (red triangles) or partially crystalline (green squares) as-quenched structure. The compositions analyzed in the present paper are marked with circles.

2. Materials and methods

(FeCoCrNi)(B,Si) master alloys were produced by arc-melting of pure elements: Iron sheet (99.9 wt%), Cobalt lumps (99.5 wt%), Chromium lumps (99.95 wt%), Nickel wire (99.98 wt%), Boron lumps (99 wt%), and Silicon lumps (99.999 wt%). The compositions studied in this work are $Fe_{20}Co_{20}Cr_{20}Ni_{20}B_{20}$, $Fe_{20}Co_{20}Cr_{20}Ni_{20}B_{15}Si_5$, $Fe_{20}Co_{20}Cr_{20}Ni_{20}B_{10}Si_{10}$, $Fe_{18.75}Co_{18.75}Cr_{18.75}Ni_{18.75}B_{10}Si_{15}$ and $Fe_{17.5}Co_{17.5}Cr_{17.5}Ni_{17.5}B_{10}Si_{20}$, labeled as AB20, AB15Si5, AB10Si10, AB10Si15 and AB10Si20, respectively. For comparison purposes the B and Si free $Fe_{25}Co_{25}Cr_{25}Ni_{25}$ HEA (in this article labeled as alloy A) was also produced. The arc-melting process was performed on a water-cooled copper plate in a Ti-gettered argon atmosphere to avoid oxidation. The master alloys were re-melted three times to assure the compositional homogeneity. Afterwards, amorphous ribbons were prepared from the alloys by melt spinning at a linear speed of 40 m s^{-1}. The thickness and the width of the resulting ribbons were of 20–30 μm and 4 mm, respectively. For the study of the mechanical properties as a function of structural state, the as-cast ribbons of AB20 and AB10Si10 were annealed at different temperatures (673, 723, 773, 823, 873, 923, 973 K) with a heating rate of 6 K min^{-1}, under a flow of Nitrogen, keeping the samples at the maximum temperature for 60 min and then cooling it down to room temperature at a cooling rate of 6 K min^{-1}. Differential Scanning Calorimetry (DSC) was performed in a NETZSCH DSC 404 with a heating rate of 20 K min^{-1} under N_2 atmosphere with flow rate of 50 mL min^{-1}.

The structural and compositional properties of the samples were investigated by Synchrotron Powder X-Ray Diffraction (XRD) at the MSPD beamline of ALBA Synchrotron [21] with an incident monochromatic wavelength of 0.4246 Å focused down to 20 × 20 μm^2(FWHM). The crystallization of the samples was studied in-situ using a Linkam hot stage, refrigerated with a closed circuit of water and the sample open to the air to maximize the angular range of the spectra and avoid artifacts from the scattering of the Linkam windows. The samples were heated at 20 K min^{-1} from room temperature up to 793 K (the maximum temperature achieved by the hot stage), held at this temperature for 2 h and cooled down to room temperature at 100 K min^{-1}. Patterns were collected with a time acquisition of 1s every 5 s using a Rayonix CCD detector. A diffraction without sample was taken at room temperature to have the background signal. The diffraction pattern at each temperature and the one of the background has been subtracted after intensity normalization. The diffraction was performed on the as-quenched ribbons; this may introduce some artifacts in the detected intensities of the Bragg reflections due to possible texture of the growing crystalline phases. However, the production of powder for the XRD analysis was discarded in order to avoid structural changes originated due to the milling process.

Scanning Electron Microscopy (SEM) was carried out in a Zeiss NEON 40 device and the images were analyzed using ImageJ software [22]. The mechanical properties of all the HEMGs, were investigated by nanoindentation from where hardness (H) and reduced Young's modulus (E_r) values were extracted using the method of Oliver and Pharr and averaging the results from 15 indentations. In particular, the hardness is defined as $H=P_{max}/A$, where A is the projected contact area and the reduced elastic modulus E_r is obtained by:

$$E_r = \frac{\sqrt{\pi}}{2\beta}\frac{s_w}{\sqrt{A}}$$

where β is a constant dependent on the geometry of the indenter tip (β = 1.034 for a Berkovich indenter). The elastic energy was determined by integrating the unloading response over the range h_{max} to h_r and the plastic energy was calculated from the area enclosed between the loading and unloading curves. The indentations were performed using an Anton-Paar, NHT^2 model, nanoindenter armed with a Berkovich

pyramidal-shaped diamond tip. The maximum applied load was 10 mN with a holding time of 5 s (30 s loading, 5 s holding and 30 s unloading), with loading/unloading rates of 20 mN min^{-1}. The thermal drift was kept below 0.005 nm s^{-1}.

3. Results and discussion

3.1. Thermal characterization

All the samples characterized in this study were completely amorphous in their as-quenched state except AB10Si20, in which XRD shows some crystalline peaks perceptible over the amorphous halo (as can be observed in [15] and also in Fig. 7 in section 3.2). This particular sample is then composed of a small fraction of crystalline particles embedded in the amorphous matrix. The analysis of the DSC curves (Fig. 2) shows a different crystallization behavior depending on the B and Si contents. AB20 shows a fast crystallization process and a second exothermic reaction at much higher temperatures. AB15Si5 and AB10Si10 show a crystallization reaction split in two peaks, while AB10Si15 shows a single crystallization event at higher temperatures. The broader and smaller exothermic event for the AB10Si20 composition is a consequence of the existence of already formed nanocrystalline particles in the as-quenched ribbons as detected by XRD (see Fig. 7). Besides the number of crystallization events, the presence of Si in the samples also changes the temperatures of the first and second crystallizations. The difference between the two processes is maximum in AB20 composition while they are almost overlapped in AB15Si5 and AB10Si10.

We can quantify the glass forming ability (GFA) and the thermal stability against crystallization by the reduced glass transition temperature $T_{rg} = T_g/T_m$ (where T_g and T_m are the glass transition and melting temperatures, respectively) and the supercooled liquid region $\Delta T_x = T_{x1}\text{-}T_g$, respectively. The computed values obtained from the DSC curves are shown in Table 1. As an example of such determination, Fig. S1 of the supplementary materials shows a magnified view of the region around T_g in sample AB10Si15 and the tangent lines used to find the T_g value. The values of T_{rg} are in the range between 0.5 and 0.6. These relatively low values indicate that these compositions are not likely to be produced as bulk metallic glasses. One exception is the AB10Si15 sample that presents a slightly higher value. This sample is also the one that shows a higher resistance to crystallization with the maximum value of ΔT_x. These results suggest that the compositional range maximizing GFA is found for a total metalloid content between 20 and 25 at% and a ratio of Si/B contents between 3/2 and 2/3.

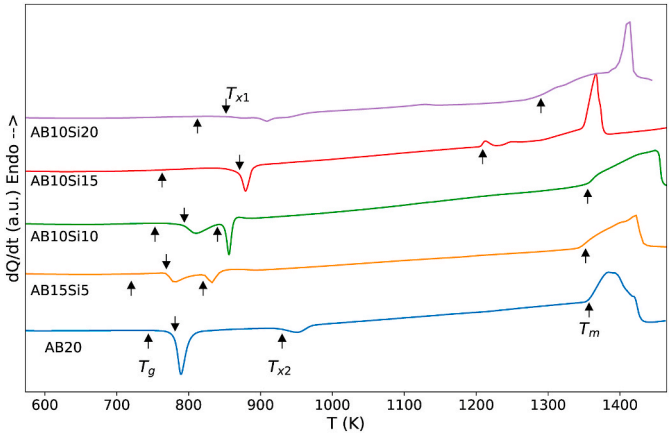

Fig. 2. DSC of the as quenched samples applying a heating rate of 20 K min^{-1}. The label of the samples indicates their B content (10,15,20 at%) and Si content (0,5,10,15,20 at%), being A = FeCoCrNi.

3.2. In-situ crystallization

The crystallization of the samples was analyzed in order to assess the role of Si and B and characterize the emerging phases. According to the value of the ratio η = Si/B, and the DSC signal (Fig. 2) we can distinguish two different regions. For $\eta \leq 1$, there are two crystallization events below 873 K, except for $\eta = 0$, where the second crystallization occurs above 873 K. For values of η larger than 1, there is only one crystallization event and, for $\eta = 2$ the crystals are already present in the as-quenched sample. The in-situ crystallization was monitored in a Linkam hot-stage. The thermal protocol followed to crystallize the samples was the following: 1) heating ramp of 20 K min^{-1} from room temperature up to 793 K; 2) isothermal annealing at 793 K for 120 min; 3) cooling to room temperature at 100 K min^{-1}.

Fig. 3 shows the crystallization for the case $\eta = 0$. The left panel shows the evolution of the intensity of the diffraction peaks with the temperature. The amorphous character of the as-quenched state is clearly seen by the low intensity of the broad peak between 10 and 15°. This broad peak is replaced by sharp lines at temperatures close to 790 K signaling the nucleation and growth of the crystalline phases. The continuity of the lines indicates the existence of only one crystallization event while the increase in brightness of the lines shows the increase in volume fraction of the crystalline phases. There is not any signature of new phases in addition to the ones appearing at 790 K. Therefore, with a holding time of 120 min at 793 K the second crystallization event detected by DSC is not reached in the X-ray diffractograms.

The right panel of Fig. 3 shows the intensity versus the diffraction angle for selected temperatures. The crystallization pattern is complex with multiple low intensity peaks. The main phases that can be identified are a solid solution with an FCC structure, the observed peaks correspond to (111), (200), (220) and (311) reflections, and two borides: Fe_3B and CoB. However, the intrinsic chemical disorder characteristic of high-entropy alloys tends to produce crystalline phases with a mixture of the main elements, thus it can be expected that the Fe_3B and CoB phase contain other metal elements. This complexity of the crystalline phases was previously analyzed in detail by Mössbauer spectroscopy [15], showing that the Mössbauer spectra of the boride phases presented hyperfine parameters that differed from the ones corresponding to a pure Fe-boride phase, thus confirming the presence of other elements (Cr, Co or Ni) in the structure. The overall structure of the phases can be identified but, similarly to other works in this type of materials [23,24], the exact distribution of metal atoms inside the borides (or silicides in the case of Si containing samples below) cannot be determined by the techniques used in this study. Besides the two identified borides, the three more intense peaks between 18 and 20° can be attributed to a more complex boride close to the Fe_3Ni_3B structure and to the intermetallic phase Cr_3Ni_2, although the identification of this latter phase is ambiguous. Thus, the first crystallization can be summarized in the following way:

$$\eta = 0\text{: amorphous} \rightarrow \text{FCC} + \text{MB} + M_3B + M_6B$$

where M stands for metallic atoms. As explained before, in this experiment the second crystallization event observed by DSC cannot be reached. However, in ref. [15] it was shown that increasing the temperature induces the formation of an M_2B phase and the disappearance of the M_3B phase.

The crystallization for the case $\eta = 1/3$ can be seen in Fig. 4. The 2D map clearly shows that two crystallization processes take place in this composition. Firstly, the amorphous phase crystallizes in a BCC structure, likely a solid solution, with the peaks at 12, 17 and 21° corresponding to the reflections (110), (200) and (211), respectively. After reaching the maximum temperature in the furnace, the second crystallization takes place with the nucleation and growth of an FCC structure together with two borides, CrFeB and FeB. There is no clear set of peaks that can be ascribed to a silicide phase, thus it is reasonable to assume

Table 1
The glass transition temperature (T_g), onset of the first crystallization event (T_{x1}), melting temperature (T_m), supercooled liquid region (ΔT_x) and reduced glass transition temperature (T_{rg}) for the completely amorphous samples, indicating label and the Si/B ratio η.

Alloy	Label	η	T_g (K)	T_{x1} (K)	T_m (K)	ΔT_x (K)	T_{rg}
FeCoCrNi	A	–	–	–	–	–	–
$(FeCoCrNi)_{80}B_{20}$	AB20	0	744	788	1353	44	0.55
$(FeCoCrNi)_{80}B_{15}Si_5$	AB15Si5	1/3	720	769	1337	41	0.54
$(FeCoCrNi)_{80}B_{10}Si_{10}$	AB10Si10	1	753	810	1349	57	0.56
$(FeCoCrNi)_{75}B_{10}Si_{15}$	AB10Si15	3/2	763	871	1203	108	0.63
$(FeCoCrNi_{70}B_{10}Si_{20}$	AB10Si20	2	812	852	1278	–	–

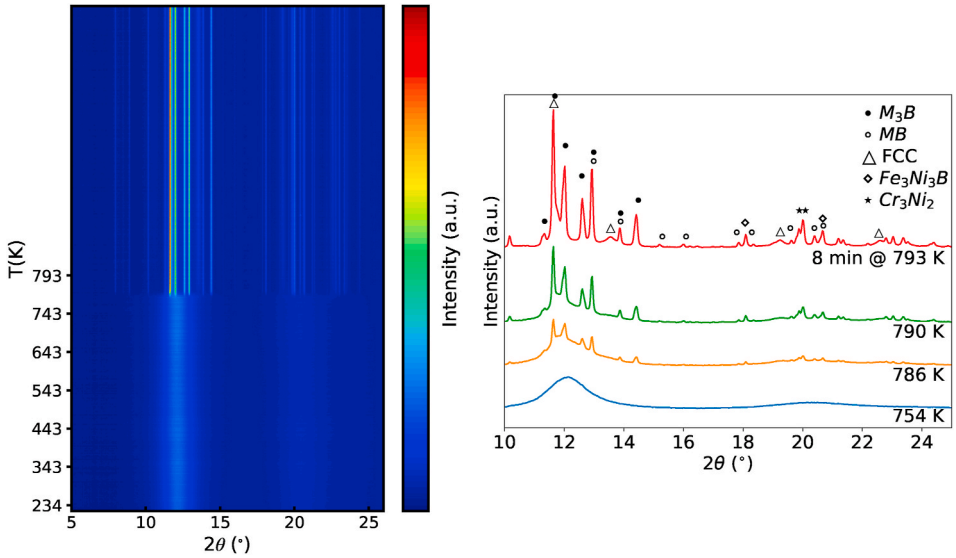

Fig. 3. Crystallization of the AB20 sample (η = 0). Left panel: 2D map of the crystalline peaks showing their intensity (in a color scale) versus the diffraction angle 2θ (x axis) and the temperature T (y axis). Right panel: diffractograms of selected temperatures, from the initial amorphous phase to the highest temperature with phase identification.

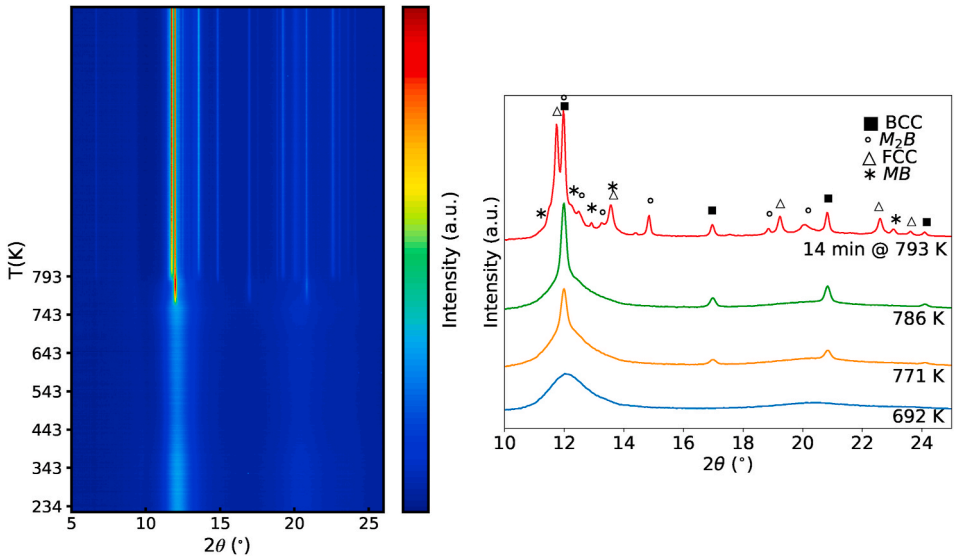

Fig. 4. Crystallization of the AB15Si5 sample (η = 1/3). Left panel: 2D map of the crystalline peaks showing their intensity (in a color scale) versus the diffraction angle 2θ (x axis) and the temperature T (y axis). Right panel: diffractograms of selected temperatures from the initial amorphous phase to the highest temperature with phase identification.

that the small amount of Si atoms is present in the other crystalline phases or in a residual amorphous fraction. The crystallization path for this case is, thus:

$$\eta = 1/3\text{: amorphous} \rightarrow \text{BCC} \rightarrow \text{BCC} + \text{FCC} + \text{MB(Si)} + \text{M}_2\text{B(Si)}$$

where (Si) means the possible presence of this element in the structure, although not confirmed.

The composition with η = 1 also presents a double crystallization

reaction (see Fig. 5). The first one takes places below 793 K and, like the previous composition, it can be ascribed to a solid solution with a BCC structure. However, contrary to $\eta = 1/3$, in the case of $\eta = 1$ there is a simultaneous crystallization of boride and silicide phases. In particular, peaks corresponding to Fe_2B, Ni_2Si and $Cr_{1.64}Fe_{0.35}B_{0.96}$ can be identified and can be globally identified as phases with an $M_2(B,Si)$ structure, although some of the peaks can also be ascribed to a Co_2B phase. The second crystallization event maintains the previous phases and it induces the nucleation and growth of a solid solution with an FCC structure, resulting in the following global crystallization path:

$\eta = 1$: amorphous → BCC + M_2(B,Si) → BCC + FCC + M_2(B,Si)

The last of the studied compositions with a completely amorphous structure in the as-quenched state corresponds to the case $\eta = 3/2$ and, contrary to the previous cases, it only presents one crystallization event in Fig. 2. From the 2D map of Fig. 6 it could seem that there are two different crystallization stages, however, looking at the selected diffractograms in the right side panel it can be seen that all the peaks are already present at the beginning of the crystallization, although some of them are masked by the halo corresponding to the amorphous matrix in which the crystalline phases grow. In a similar way than in the case $\eta = 1$, the main existing crystalline phase is a solid solution with a BCC structure that grows simultaneously with borides and silicides. In particular, the peaks can be identified with Ni_2Si and Cr_2B phases. The peaks at around 11° and 17° are not identified but can be compatible with Fe_5Si_3 or Ni_3Si phases if some texture is assumed. Unlike the other compositions with less Si, in this case there is no growth of an FCC structure. What it can be observed, however, is that after a relatively short time at 793 K (approximately 30 min) the peaks corresponding to the BCC solid solution begin to decrease in intensity at the expenses of borides and silicides. Therefore, in this composition the crystallization path is more simple and can be summarized as follows:

$\eta = 3/2$: amorphous → BCC + M_2(Si,B)

The last of the studied compositions corresponds to the case $\eta = 2$, which is partially crystalline in the as-quenched state, although the majority of the as-quenched structure remains amorphous (see Fig. 7). Despite this double character of the structure, the study of the crystalline phases is interesting in order to have a better picture of the effect of Si in the crystallization path of this family of HEMGs. The crystals present in the as-quenched state can be identified as a solid solution with a BCC structure that continuously grows when increasing temperature. After the full treatment of the sample (120 min at 793 K) besides the BCC phase, several peaks appear that are compatible with a Ni_2Si phase. There are no clear peaks corresponding to borides, although the peaks at 11.4° and 12.2° are consistent with a Ni_2B phase. Thus, the crystallization path is:

$\eta = 2$: amorphous + BCC → BCC + M_2(Si, B)

Summarizing, the analyzed crystallization paths show a clear trend with the Si content. When there is no Si present in the HEMG ($\eta = 0$) the system crystalizes in an FCC structure together with a complex combination of borides, including a metastable M_3B phase, and some intermetallic phases. Adding Si ($\eta > 0$) changes the structure of the principal crystalline phase, that now is BCC instead of FCC. Moreover, the first boride to crystallize is no longer the metastable M_3B but the stable M_2B. In the compositions with two crystallization events ($\eta \leq 1$), the second crystallization induces the growth of the FCC structure that coexists with the BCC phase. In the compositions with low Si content ($\eta = 1/3$), there is also the formation of MB phase. Increasing the Si content ($\eta = 1$) implies the crystallization of only M_2B and M_2Si phases. Finally, for the compositions with the highest Si content ($\eta = 3/2$ and $\eta = 2$) the second crystallization disappears obtaining a microstructure composed only of a BCC solid solution and M_2(B,Si) crystals.

3.3. Nanoindentation

Fig. 8 (left) shows the load-displacement curves of all the samples in the as-quenched state, including composition A for reference. In addition to the different penetration depths, the slope of the unloading part of the indentation curves, related to the contact stiffness, indicates a different value of the reduced Young's modulus (E_r). From these curves the hardness (H) and E_r can be calculated and the values are shown in Table 2.

Fig. 8 (right) shows the change of these magnitudes as a function of the composition for the as-quenched samples. The large increase in hardness from the base composition (~ 4 GPa) to the B and Si containing alloys (~14–18 GPa) can be explained by the strong nature of the (B,Si)-M interatomic bonds and the change from an FCC to an amorphous structure, where the absence of long-range order and crystalline defects increases the resistance to plastic deformation. There is no

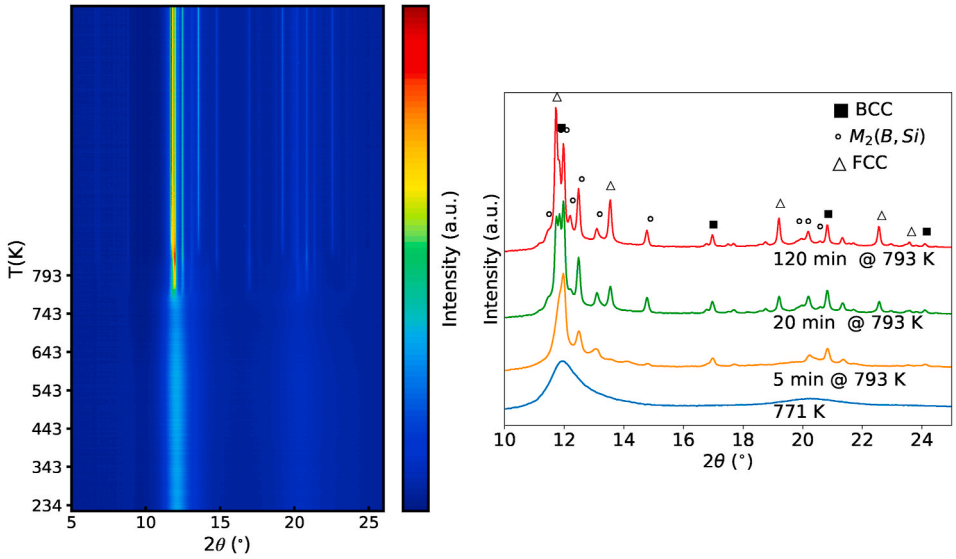

Fig. 5. Crystallization of the AB10Si10 sample ($\eta = 1$). Left panel: 2D map of the crystalline peaks showing their intensity (in a color scale) versus the diffraction angle 2θ (x axis) and the temperature T (y axis). Right panel: diffractograms of selected temperatures from the initial amorphous phase to the highest temperature with phase identification.

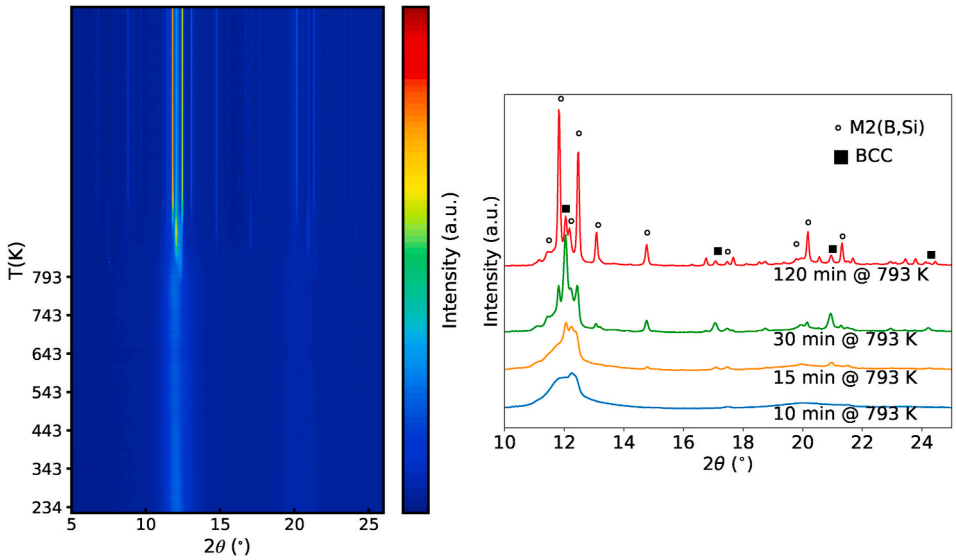

Fig. 6. Crystallization of the AB10Si15 sample (η = 3/2). Left panel: 2D map of the crystalline peaks showing their intensity (in a color scale) versus the diffraction angle θ (x axis) and the temperature T (y axis). Right panel: diffractograms of selected times after reaching the maximum temperature in the hot stage.

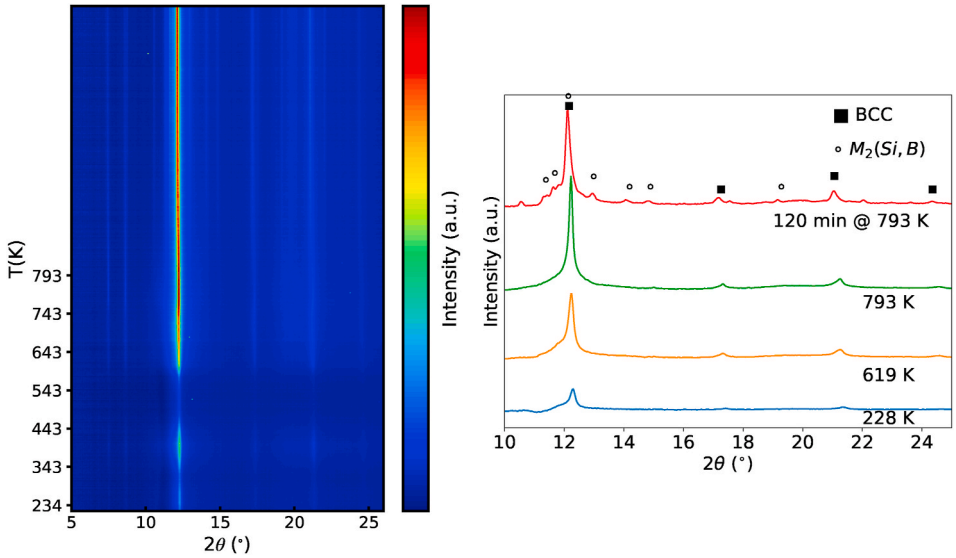

Fig. 7. Crystallization of the AB10Si20 sample (η = 2). Left panel: 2D map of the crystalline peaks showing their intensity (in a color scale) versus the diffraction angle θ (x axis) and the temperature T (y axis). Right panel: diffractograms of selected temperatures from the initial partially crystalline phase to the highest temperature with phase identification.

clear trend in the values of H or E_r as a function of composition, all amorphous samples showing outstanding high hardness values, three times as hard as stainless steels [25].

However, the highest values of these magnitudes are found for AB10Si20, i.e. the alloy that has the major content of B and Si and, in addition, contains some nanocrystals embedded in its amorphous structure (as seen in Fig. 13 of reference [15] and in Fig. S2 of the supplementary materials). It is expected that the elastic properties of a material are related to its atomic bonding in a way that compositions with stronger bonds exhibit higher values of E_r [26]. There are two possible contributions to the maximum values of H and E_r in the AB10Si20 alloy. On the one hand, the large amount of Si creates stronger covalent bonds between this element and the metallic elements [27,28]. On the other hand, the mechanical properties can be enhanced in glass/nanocrystalline composites due to the role of nanocrystals in hindering shear band propagation [29,30]. In addition, in the case of AB10Si20, the precipitation of the BCC phase rises the content of Si and B in the remaining amorphous phase, thus increasing the hardness of the glass matrix.

It is interesting to compare the hardness and elastic modulus values of the as-quenched alloys studied here with other high-entropy alloys of similar compositions probed also by nanoindentation [31,32]. In these references the maximum loads were between 10 and 30 mN, similar to the ones in the present work, although some differences could be expected due to the measures were done at a strain rates of $5 \times 10^{-2}\,s^{-1}$ in the case of ref. [31]. Fig. 9 displays the values of the Young's modulus versus hardness for several alloys that also contain Fe, Co and Cr in the base composition and additions of other elements like, Cu, Si or Al to tailor their properties. From this figure, it is clear that the microalloying with Al and the incorporation of Mn in the base composition are beneficial for the elastic modulus but it produces only a moderate increase in the hardness. All these compositions present a diversity of microstructures depending on the particular composition and alloying element and comprise FCC, BCC, mixture of BCC and FCC and also a mixture of FCC

Table 2
Hardness (H), reduced Young's modulus (E_r), plastic energy (U_p), elastic energy (U_{el}), wear resistance (H/E_r) and elastic recovery (U_{el}/U_{tot}) measured by nanoindentation.

Samples	H (GPa)	E_r (GPa)	U_p (nJ)	U_{el} (nJ)	U_{tot} (nJ)	H/E_r	U_{el}/U_{tot}
A	4.1 (2)	122 (5)	1.04 (3)	0.247 (8)	1.28 (4)	0.034 (2)	0.19 (2)
AB20	14.4 (6)	167 (5)	0.353 (2)	0.343 (2)	0.69 (1)	0.086 (5)	0.49 (1)
AB15Si5	12.5 (5)	150 (7)	0.405 (6)	0.351 (2)	0.75 (1)	0.084 (6)	0.46 (1)
AB10Si10	15.5 (6)	162 (2)	0.367 (7)	0.356 (3)	0.72 (1)	0.095 (3)	0.49 (1)
AB10Si15	12.6 (4)	155 (2)	0.401 (2)	0.345 (2)	0.74 (3)	0.081 (3)	0.46 (1)
AB10Si20	17.7 (7)	176 (4)	0.28 (2)	0.361 (2)	0.64 (2)	0.100 (5)	0.56 (3)

and HCP phases. The composition with the highest elastic modulus is Al_3(FeCoCrNiCu) that consists of a BCC phase in a dendritic configuration. The addition of B and/or Si extraordinarily improves the hardness, while the change in the elastic modulus is less significant. This increase of hardness opens a new route to design new high-entropy alloys with improved properties seeking for a combination of constituent elements capable to induce amorphous structures.

In order to study the effect of nanocrystallization on the mechanical properties, two of the compositions, AB20 and AB10Si10, were selected. These two alloys have the same total atomic content of metalloids but different Si/B ratio, thus we consider them as representative of the whole set of samples. As discussed above, they show different crystallization reactions, forming FCC or BCC crystals respectively at the initial stages. The samples were annealed up to different temperatures, from below the glass transition up to full crystallization. It is well known that below T_g a heat treatment causes changes in the physical and mechanical properties of glasses due to structural relaxation. The decrease of excess free volume during this process causes a reduction of atomic mobility and an increase of Young's modulus and hardness [26,33–35].

The results of H and E_r for the two compositions are shown in Fig. 10 and are detailed in Table 3. Fig. 10 (left), corresponding to AB20, shows a progressive increase of both H and E_r up to the annealing at 773 K. According to our previous characterization [15], after annealing at 773 K the sample is composed of nanocrystals (FCC and M_3B) embedded in an amorphous matrix. At this point, the maximum values of the hardness and reduced Young's modulus are reached, being 24 GPa and 215 GPa, respectively. The increase of such mechanical properties between the as-quenched and the annealed amorphous samples can be attributed to the annihilation of excess free volume associated to the structural relaxation of the glass [35]. At higher annealing temperatures, the crystallization of the hard M_3B phase also contributes to the increase in the strength of the sample [28]. At annealing temperatures higher than 773 K, E_r remains almost constant while the hardness decreases. The final state of the sample is composed by FCC crystals together with the stable boride M_2B. The decrease in hardness can be explained by the growth of the FCC phase which has low hardness compared to the amorphous state. With increasing the annealing temperature, the hardness decreases gradually as the grain growth of the FCC phase occurs [36]. The average size of the crystalline grains changes from 70 nm at 773 K up to 185 nm at 973 K [15]. Thus, the decrease of the hardness can be explained by the conventional Hall-Petch equation [37] that predicts an increase of the strength with decreasing grain size due to dislocation pile-up at grain boundaries.

For the AB10Si10 alloy, Fig. 10 (right), the data shows a more complex behavior. The hardness and reduced elastic modulus increase up to a clear maximum that occurs when annealing at 723 K, before the crystallization onset. At higher annealing temperatures, both H and E_r decrease during the first crystallization step where a BCC solid solution together with an M_2(B,Si) phase appear [15]. In the second crystallization step, in which the BCC phase is replaced by FCC, E_r increases again. The decrease of both hardness and modulus at the final stages of the crystallization can be attributed to the grain growth of the FCC phase. Therefore, in the AB10Si10 material, the maximum value of the hardness occurs for a fully amorphous, although structurally relaxed, structure.

More information can be extracted from the ratio between hardness and reduced elastic modulus (H/E_r), and from the elastic recovery, i.e.

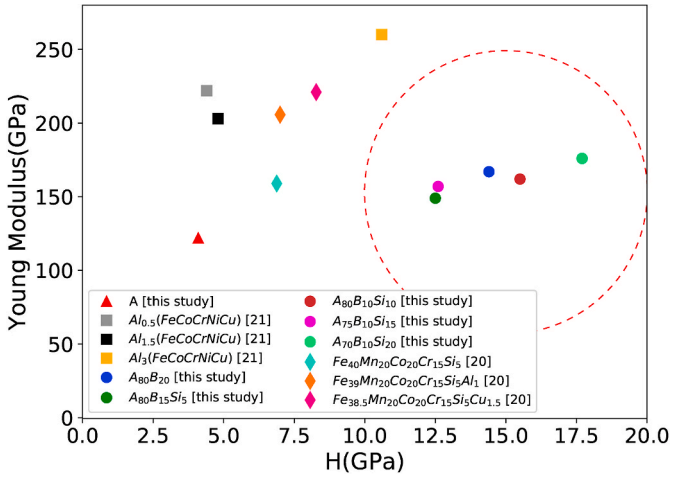

Fig. 9. Comparison of Young modulus and hardness for several compositions [31,32]. The circle indicates the compositions investigated in this study.

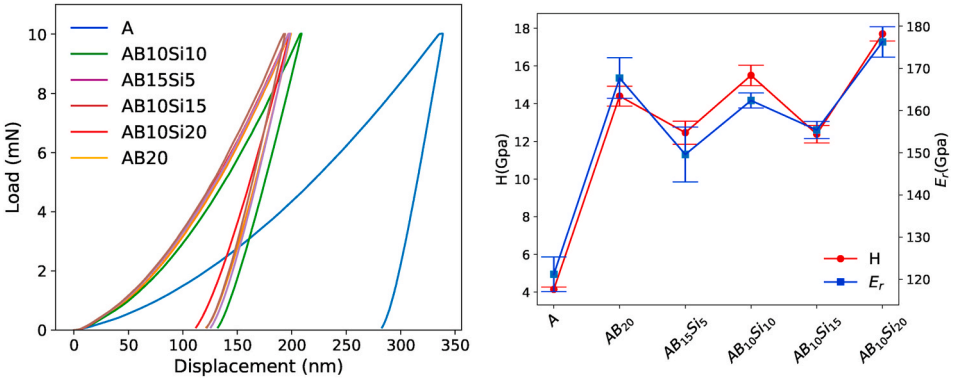

Fig. 8. Load-displacement of nanoindentation curves (left) and variation of hardness (H) and reduced Young's modulus (E_r) (right) for as quenched ribbons at room temperature.

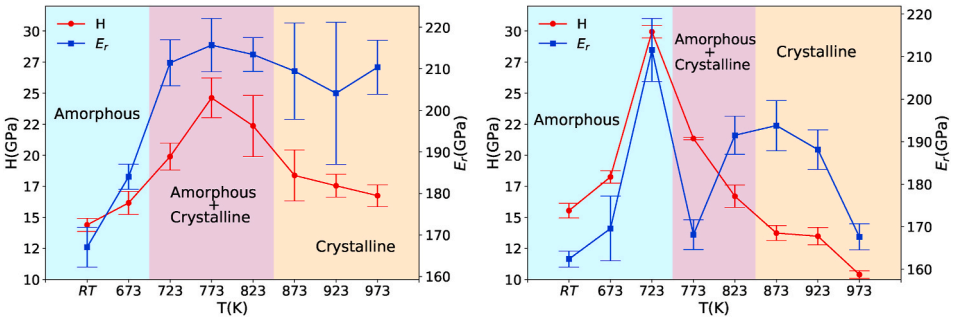

Fig. 10. Variation of hardness (H) and reduced elastic modulus (E_r) as a function of annealing temperature for AB20 (left) and AB10Si10 (right).

Table 3
Hardness (H), reduced Young's modulus (E_r), plastic energy (U_p), elastic energy (U_{el}), wear resistance (H/E_r) and elastic recovery (U_{el}/U_{tot}) measured by nano-indentation for AB20 and AB10Si10 samples for different annealing temperatures.

T (K)	H (GPa)		E_r (GPa)		U_p (nJ)		U_{el} (nJ)		U_{tot} (nJ)		H/E_r		U_{el}/U_{to}	
	AB20	AB10Si10	AB20	AB10Si10	AB20	AB10Si10	AB20	AB10Si10	AB20	AB10Si10	AB20	AB10Si10	AB20	AB10Si10
aq	14.5 (6)	15.6 (6)	167 (5)	162 (2)	0.353 (2)	0.3 (2)	0.343 (2)	0.43 (9)	0.696 (4)	0.7 (2)	0.086 (6)	0.095 (4)	0.492 (5)	1 (2)
673	16.1 (2)	18.3 (5)	184 (3)	170 (8)	0.341 (8)	0.329 (7)	0.326 (3)	0.372 (3)	0.67 (2)	0.70 (1)	0.087 (1)	0.107 (7)	0.49 (2)	0.53 (2)
723	20 (2)	29.9 (5)	211 (6)	212 (8)	0.276 (5)	0.296 (6)	0.329 (2)	0.382 (4)	0.605 (7)	0.68 (1)	0.094 (7)	0.141 (7)	0.54 (1)	0.56 (2)
773	25 (2)	21.3 (2)	216 (7)	168 (4)	0.198 (6)	0.198 (6)	0.382 (3)	0.382 (3)	0.58 (1)	0.58 (1)	0.11 (1)	0.126 (3)	0.66 (2)	0.66 (2)
823	22 (3)	16.7 (9)	213 (5)	192 (5)	0.247 (2)	0.318 (4)	0.345 (3)	0.330 (2)	0.59 (2)	0.648 (6)	0.10 (2)	0.087 (6)	0.58 (2)	0.509 (7)
873	18 (3)	13.7 (6)	210 (20)	194 (6)	0.307 (5)	0.384 (5)	0.316 (2)	0.302 (3)	0.623 (7)	0.686 (8)	0.09 (1)	0.069 (5)	0.507 (8)	0.44 (1)
923	17.5 (2)	13.5 (7)	200 (20)	188 (5)	0.301 (5)	0.394 (8)	0.352 (3)	0.302 (6)	0.653 (8)	0.70 (2)	0.085 (7)	0.071 (5)	0.54 (1)	0.43 (2)
973	16.7 (2)	10.4 (3)	210 (7)	168 (3)	0.327 (7)	0.472 (2)	0.307 (2)	0.307 (5)	0.634 (9)	0.779 (7)	0.079 (2)	0.062 (2)	0.48 (1)	0.39 (1)

the ratio between the elastic energy (U_{el}) and the total energy (elastic plus plastic, U_p) [33,38]. The H/E_r ratio is related to the elastic strain to failure and it is a suitable parameter to describe the wear resistance of the sample [17,39]. These values for all the analyzed compositions are shown in Table 2, while for all the annealing temperatures of samples AB20 and AB10Si10 are shown in Table 3. Among all the studied compositions, AB10Si20 shows the highest wear resistance and elastic recovery, showing that the presence of nanocrystals and larger amount of metalloid percentage helps to improve these mechanical properties. For the completely amorphous samples, AB10Si10 is the one with the better wear resistance, while all have similar values of the elastic recovery. Focusing on compositions AB20 and AB10Si10 annealed at different temperatures, the wear resistance shows a similar behavior as the hardness, being maximum after annealing at 773 K for AB20 and at 723 K for AB10Si10. However, the elastic recovery is similar, around the 50%, in all cases, being maximum in the two compositions after annealing at 773 K. Thus, the combination of nanocrystals and a relaxed amorphous matrix yields the best performance in terms of energy recovery.

The analysis of the SEM images of the indents yields information of the sink-in and pile-up phenomena [40]. Pile-up effect happens when the surface is indented heavily and the localized plastic deformation zone pushes upward the surrounding material. On the other hand, sink-in happens when the plastic zone tends to shift away from the indented area. In crystalline materials, the formation of pile-up along a specific directional line around the indent can be related to the crystallographic orientation and to the crystal symmetry [41]. The method of Oliver and Pharr to compute the hardness does not consider the effect of pile-up and it can induce an overestimation of the calculated hardness [42] and also influences the elastic modulus determination by changing the contact area. In Fig. 11 the SEM image of a typical indentation of AB20 annealed at 873 K is shown in the inset, together with the projected and the pile-up area calculated using ImageJ software. Additional SEM images of both samples (AB20 and AB10Si10) at selected temperatures are shown in Fig. S3 of the supplementary materials.

Fig. 11 shows the fluctuation of the pile-up area as a function of the

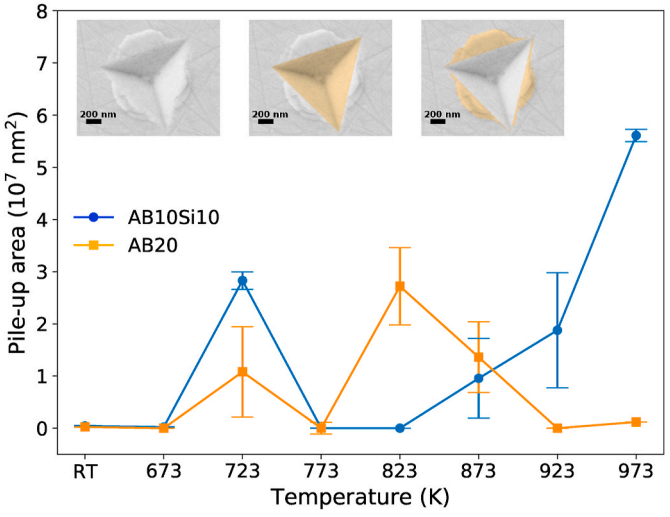

Fig. 11. Measured pile-up area for different annealing temperatures for the AB20 and AB10Si10 samples. In the inset, typical SEM image of an indentation in the AB20 sample (left), definition of the area to compute the projected area in yellow (middle) and the pile-up area in yellow (right).

annealing temperature for samples AB20 and AB10Si10. It can be seen that in both samples there is no formation of pile-up until annealing at 723 K. At this temperature, the structure is mainly amorphous although the AB20 sample contains some fraction of nanocrystals. The plastic deformation of amorphous metals involves an increase of the internal free volume. This effect is less pronounced in the as-quenched samples which already contain a large amount of free volume. At higher annealing temperatures the behavior of the two compositions is different. For the AB20 sample, the pile-up reaches its maximum at the end of the first crystallization at 823 K. At this temperature, the structure consists of an FCC solid solution together with the M_3B phase. As the crystallization progress and this boride is replaced by M_2B and the FCC grains grow, the pile-up area steadily decreases. On the contrary, for the AB10Si10 sample, after an increase of the pile-up as the amorphous structure relaxes before crystallization, the pile-up area is reduced to zero during the first crystallization event in which the structure consists mainly of BCC and M_2(B,Si) phases. As the BCC is replaced by the FCC one, the pile-up area continuously grows until reaching its maximum value in the fully crystallized sample. The effect of the pile-up is higher on the hardness than on the elastic modulus because the first is inversely dependent on the area while the second on the square root of the area. The pile-up effect increases when the strain hardening exponent decreases [43]. Therefore, the fully crystallized samples of AB10Si10 behave more plastically than the AB20 composition. However, for the samples annealed only up to the first crystallization, where AB20 sample contain the M_3B phase, the behavior is reversed, being more plastic this composition than the AB10Si10 alloy.

Some overestimation of H could happen due to the formation of the pile-up. In a latter article [44], Oliver and Pharr reviewed the limitations of their original model and noticed that a convenient parameter that illustrates the possible influence of pile-up formation on the mechanical properties is the ratio h_f/h_{max}, which is independent of the indentation depth in self-similar geometries, such as the Berkovich indenter. For conical or Berkovich indenters, when this ratio is smaller than 0.7, like in the present case, the little pile-up observed does not have a strong influence on the obtained results. Conversely, their original method becomes more inaccurate for $h_f/h_{max} > 0.7$.

4. Conclusions

In this paper we have studied a new family of high entropy metallic glasses characterizing the structure by X-ray diffraction and the mechanical properties by nanoindentation. The main results obtained can be summarized as follows:

- An addition of 10 at% of B and 15 at% of Si to the base equiatomic FeCoCrNi composition maximizes the glass forming ability and thermal stability of the amorphous phase.
- For Si/B ratios lower or equal than one the alloys present two crystallization events while for higher values of this ratio there is only one crystallization peak. Moreover, as the amount of Si increases the main crystalline phase changes from FCC to BCC.
- The amorphous samples show an outstanding hardness due to the strong nature of the (B,Si)-M bonds and the absence of crystalline structure. However, the amorphous samples with relaxed structure and nanocrystalline inclusions show further enhancement of these mechanical properties.
- The evaluation of the mechanical properties as a function of the annealing temperature reveals that the higher values of hardness are found in a structure composed of nanocrystals embedded in a relaxed amorphous matrix in the case of the Si-free alloys and in a relaxed amorphous structure in the Si-containing alloys.
- The wear resistance and elastic recovery are higher in the partially crystalline samples.

These results give the basic guidelines to design new high-entropy metallic glass alloys with tailored mechanical properties within the $(FeCoCrNi)_{100-x-y}B_xSi_y$ system. The high content of Cr is expected to give these materials a good corrosion resistance, an aspect that will be characterized in future works. The combination of wear and corrosion resistance, high hardness and the thermal stability up to relatively high temperatures point out this family of alloys as adequate materials for highly demanding applications.

Data availability

The raw/processed data required to reproduce these findings can be shared upon request to the corresponding author.

Authorship statement

All persons who meet authorship criteria are listed as authors, and all authors certify that they have participated sufficiently in the work to take public responsibility for the content, including participation in the concept, design, analysis, writing, or revision of the manuscript. Furthermore, each author certifies that this material or similar material has not been and will not be submitted to or published in any other publication before its appearance in Intermetallics.

Declaration of competing interest

The authors declare that they have no known competing financial interests or personal relationships that could have appeared to influence the work reported in this paper.

Acknowledgements

Research Project PID2020-112975 GB-I00 funded by MCIN/AEI/10.13039/501100011033. L. Panahi acknowledges the financial support from Generalitat de Catalunya through a FI grant 2018FI_B_00502. P. Bruna and E. Pineda acknowledge the financial support from Generalitat de Catalunya grant 2017-SGR-42. J. S. acknowledges the Spanish Government (grant MAT2017-86357-C3-1-R and associated FEDER) and the Generalitat de Catalunya (grant 2017-SGR-292) for financial support. X-ray diffraction experiments were performed at MSPD beamline at ALBA Synchrotron with the collaboration of ALBA staff (Alba experiment 2018022691). The authors acknowledge the priceless help of Dr. Trifon Trifonov at the facilities of the Barcelona Research Center in Multiscale Science and Engineering.

Appendix A. Supplementary data

Supplementary data to this article can be found online at https://doi.org/10.1016/j.intermet.2021.107432.

References

[1] L. Maillé, C. Sant, P. Aubert, P. Garnier, Morphological and mechanical properties study of $[WO_3/W]_n$ nanoscale multilayers, Thin Solid Films 479 (2005) 201–206. https://doi:10.1016/j.tsf.2004.11.203.
[2] Y.Y. Chen, T. Duval, U.D. Hung, J.W. Yeh, H.C. Shih, Microstructure and electrochemical properties of high entropy alloys-a comparison with type-304 stainless steel, Corrosion Sci. 47 (2005) 2257–2279. https://doi:10.1016/j.corsci.2004.11.008.
[3] P. Koželj, S. Vrtnik, A. Jelen, S. Jazbec, Z. Jagličić, S. Maiti, M. Feuerbacher, W. Steurer, J. Dolinšek, Discovery of a superconducting high-entropy alloy, Phys. Rev. Lett. 113 (2014) 107001. https://doi:10.1103/PhysRevLett.113.107001.
[4] B. Gludovatz, A. Hohenwarter, D. Catoor, E.H. Chang, E.P. George, R.O. Ritchie, A fracture-resistant high-entropy alloy for cryogenic applications, Science 345 (2014), 1153-1148, https://doi:10.1126/science.1254581.
[5] H.F. Li, X.H. Xie, K. Zhao, Y.B. Wang, Y.F. Zheng, W.H. Wang, L. Qin, In vitro and in vivo studies on biodegradable CaMgZnSrYb high-entropy bulk metallic glass, Acta Biomater. 9 (2013) 8561–8573. https://doi:10.1016/j.actbio.2013.01.029.
[6] Y. Cai, Y. Chen, Z. Luo, F. Gao, L. Li, Manufacturing of $FeCoCrNiCu_x$ medium-entropy alloy coating using laser cladding technology, Mater. Des. 133 (2017) 91–108. https://doi:10.1016/j.matdes.2017.07.045.

[7] P. Wang, P. Huang, F.L. Ng, W.J. Sin, S. Lu, M.L.S. Nai, Z.L. Dong, J. Wei, Additively manufactured CoCrFeNiMn high-entropy alloy via pre-alloyed powder, Mater. Des. 168 (2019) 107576. https://doi.org/10.1016/j.matdes.2018.107576.

[8] T. Burgess, M. Ferry, Nanoindentation of metallic glasses, Mater. Today 12 (2009) 24–32. https://doi:10.1016/S1369-7021(09)70039-2.

[9] J. Li, W. Jia, J. Wang, H. Kou, D. Zhang, E. Beaugnon, Enhanced mechanical properties of a CoCrFeNi high entropy alloy by supercooling method, Mater. Des. 95 (2016) 183–187. https://doi:10.1016/j.matdes.2016.01.112.

[10] L.L. Xiao, Z.Q. Zheng, S.W. Guo, P. Huang, F. Wang, Ultra-strong nanostructured CrMnFeCoNi high entropy alloys, Mater. Des. 194 (2020) 108895. https://doi:10.1016/j.matdes.2020.108895.

[11] L. Zendejas Medina, M.V. Tavares da Costa, E.M. Paschalidou, G. Lindwall, L. Riekehr, M. Korvela, S. Fritze, S. Kolozsvári, E.K. Gamstedt, L. Nyholm, U. Jansson, Enhancing corrosion resistance, hardness, and crack resistance in magnetron sputtered high entropy CoCrFeMnNi coatings by adding carbon, Mater. Des. 205 (2021) 109711. https://doi:10.1016/j.matdes.2021.109711.

[12] D.B. Miracle, O.N. Senkov, A critical review of high entropy alloys and related concepts, Acta Mater. 122 (2017) 448–511. https://doi:10.1016/j.actamat.2016.08.081.

[13] I. Szlufarska, A. Nakano, P. Vashishta, A crossover in the mechanical response of nanocrystalline ceramics, Science 309 (2005) 911–914. https://doi:10.1126/science.1114411.

[14] Q. Hu, S. Guo, J.M. Wang, Y.H. Yan, S.S. Chen, D.P. Lu, K.M. Liu, J.Z. Zou, X. R. Zeng, Parametric study of amorphous high-entropy alloys formation from two new perspectives: atomic radius modification and crystalline structure of alloying elements, Sci. Rep. 7 (2017) 1–12. https://doi:10.1038/srep39917.

[15] S.L. Panahi, M. Garcia-ramón, E. Pineda, P. Bruna, New (FeCoCrNi)-(B,Si) high-entropy metallic glasses, study of the crystallization processes by X-ray di ff raction and Mössbauer spectroscopy, J. Non-Cryst. Solids 547 (2020) 120301. https://doi:10.1016/j.jnoncrysol.2020.120301.

[16] D.H. Lee, J.A. Lee, Y. Zhao, Z. Lu, J.Y. Suh, J.Y. Kim, U. Ramamurty, M. Kawasaki, T.G. Langdon, J. il Jang, Annealing effect on plastic flow in nanocrystalline CoCrFeMnNi high-entropy alloy: a nanomechanical analysis, Acta Mater. 140 (2017) 443–451. https://doi:10.1016/j.actamat.2017.08.057.

[17] L.C.R. Aliaga, J. Fornell, S. Suriñach, M.D. Baró, C.S. Kiminami, C. Bolfarini, W. J. Botta, J. Sort, Comparative study of nanoindentation on melt-spun ribbon and bulk metallic glass with $Ni_{60}Nb_{37}B_3$ composition, J. Mater. Res. 28 (2013) 2740–2746. https://doi:10.1557/jmr.2013.260.

[18] W.C. Oliver, G.M. Pharr, An improved technique for determining hardness, J. Mater. Res. 7 (1992) 1564–1583, https://doi.org/10.1557/JMR.1992.1564.

[19] L.S. Zhang, Preparation of CoCrFeNiCuMnSix high entropy alloys and their microstructure and properties, Adv. Mater. Res. 750–752 (2013) 615–618. https://doi:10.4028/www.scientific.net/AMR.750-752.615.

[20] Z. Zhang, Elastic Properties of Bulk-Metallic Glasses Studied by Resonant Ultrasound Spectroscopy, PhD Diss, University of Tennessee, 2008.

[21] F. Fauth, I. Peral, C. Popescu, M. Knapp, The New Material Science Powder Diffraction Beamline at ALBA Synchrotron, Powder Diffr., 2013. https://doi:10.1017/S0885715613000900.

[22] C.A. Schneider, W.S. Rasband, K.W. Eliceiri, NIH Image to ImageJ: 25 years of image analysis, Nat. Methods 9 (2012) 671–675. https://doi:10.1038/nmeth.2089.

[23] T. Qi, Y. Li, A. Takeuchi, G. Xie, H. Miao, W. Zhang, Soft magnetic $Fe_{25}Co_{25}Ni_{25}(B, Si)_{25}$ high entropy bulk metallic glasses, Intermetallics 66 (2015) 8–12. https://doi:10.1016/j.intermet.2015.06.015.

[24] H. Zhang, X.C. Zhong, Y.Z. He, W.H. Li, W.F. Wu, G. Chen, S. Guo, Effect of high configuration entropy and rare earth addition on boride precipitation and mechanical properties of multi-principal-element alloys, J. Mater. Eng. Perform. 26 (2017) 3750–3755. https://doi.org/10.1007/s11665-017-2831-3.

[25] X.F. Wang, X.P. Yang, Z.D. Guo, Y.C. Zhou, H.W. Song, Nanoindentation characterization of mechanical properties of ferrite and austenite in duplex stainless steel, Adv. Mater. Res. (2007) 26–28. https://doi:10.4028/www.scientific.net/amr.26-28.1165.

[26] W. Guo, P.P. Choi, J.B. Seol, Amorphous phase separation in an Fe-based bulk metallic glass, Mater. Lett. 190 (2017) 161–164. https://doi:10.1016/j.matlet.2017.01.012.

[27] K.H. Kong, K.C. Kim, W.T. Kim, D.H. Kim, K. Dh, Microstructural features of multicomponent $FeCoCrNiSi_x$ alloys, Appl. Microsc. 45 (2015) 32–36.

[28] I. Szlufarska, R.K. Kalia, A. Nakano, P. Vashishta, Atomistic mechanisms of amorphization during nanoindentation of SiC: a molecular dynamics study, Phys. Rev. B Condens. Matter 71 (2005) 1–11. https://doi:10.1103/PhysRevB.71.174113.

[29] J. Eckert, A. Kübler, L. Schultz, Mechanically alloyed $Zr_{55}Al_{10}Cu_{30}Ni_5$ metallic glass composites containing nanocrystalline W particles, J. Appl. Phys. 85 (1999) 7112–7119, https://doi.org/10.1063/1.370519.

[30] D.C. Hofmann, J.-Y. Suh, A. Wiest, G. Duan, M.-L. Lind, M.D. Demetriou, W. L. Johnson, Designing metallic glass matrix composites with high toughness and tensile ductility, Nature 451 (2008) 1085–1089. https://doi:10.1038/nature06598.

[31] S. Sinha, R.A. Mirshams, T. Wang, S.S. Nene, M. Frank, K. Liu, R.S. Mishra, Nanoindentation behavior of high entropy alloys with transformation-induced plasticity, Sci. Rep. 9 (2019) 1–11. https://doi:10.1038/s41598-019-43174-x.

[32] Y. Sun, P. Chen, L. Liu, M. Yan, X. Wu, C. Yu, Z. Liu, Local mechanical properties of $Al_xCoCrCuFeNi$ high entropy alloy characterized using nanoindentation, Intermetallics 93 (2018) 85–88. https://doi:10.1016/j.intermet.2017.11.010.

[33] Y. Cheng, C. Cheng, Relationships between hardness,elastic modulus and the work, Appl. Phys. Lett. 73 (1998) 614–616, https://doi.org/10.1063/1.121873.

[34] E. Pellicer, S. Pané, K.M. Sivaraman, O. Ergeneman, S. Suriñach, M.D. Baró, B. J. Nelson, J. Sort, Effects of the anion in glycine-containing electrolytes on the mechanical properties of electrodeposited Co-Ni films, Mater. Chem. Phys. 130 (2011) 1380–1386. https://doi:10.1016/j.matchemphys.2011.09.032.

[35] F.H. Duan, J. Pan, Y. Lin, Y. Li, Significant structural relaxation in a Mo-O binary amorphous alloy, J. Non-Cryst. Solids 514 (2019) 10–14. https://doi:10.1016/j.jnoncrysol.2019.03.038.

[36] B. Gludovatz, E.P. George, R.O. Ritchie, Processing, Microstructure and mechanical properties of the CrMnFeCoNi high-entropy alloy, JOM (J. Occup. Med.) 67 (2015) 2262–2270. https://doi:10.1007/s11837-015-1589-z.

[37] A. Leitner, V. Maier-Kiener, D. Kiener, Extraction of flow behavior and Hall–petch parameters using a nanoindentation multiple sharp tip approach, Adv. Eng. Mater. 19 (2017) 1–9. https://doi:10.1002/adem.201600669.

[38] M.T. Attaf, Connection between the loading curve models in elastoplastic indentation, Mater. Lett. 58 (2004) 3491–3498. https://doi:10.1016/j.matlet.2004.06.049.

[39] A. Leyland, A. Matthews, On the significance of the H/E ratio in wear control: a nanocomposite coating approach to optimised tribological behaviour, Wear 246 (2000) 1–11. https://doi:10.1016/S0043-1648(00)00488-9.

[40] M. Sullivan, Measuring, Evaluating, and Describing Pile-Up and Sink-In during Nanoindentation of Thin Films on Substrates, PhD diss, Auburn University, 2015.

[41] R.A. Mirshams, A.K. Srivastava, Effect of pile-up on nanoindentation measurements of polycrystalline bulk metals, Adv. Mater. Res. 853 (2014) 143–150. https://doi:10.4028/www.scientific.net/AMR.853.143.

[42] D. Beegan, S. Chowdhury, M.T. Laugier, The nanoindentation behaviour of hard and soft films on silicon substrates, Thin Solid Films 466 (2004) 167–174. https://doi:10.1016/j.tsf.2004.03.006.

[43] P. Burik, L. Pešek, L. Volesk\u00fd, Effect of pile-up on the mechanical characteristics of steel with different strain history by depth sensing indentation, Met. 2014 - 23rd Int. Conf. Metall. Mater. Conf. Proc. 2 (2014) 629–633.

[44] W.C. Oliver, G.M. Pharr, Measurement of hardness and elastic modulus by instrumented indentation: advances in understanding and refinements to methodology, J. Mater. Res. 19 (2004) 3–20, https://doi.org/10.1557/jmr.2004.19.1.3.